Characteristics of Subsurface Ocean Response to ENSO Assessed from Simulations with the NCEP Climate Forecast System

HUI WANG

Climate Prediction Center, NOAA/NWS/NCEP, College Park, Maryland, and Wyle Science, Technology and Engineering Group, Houston, Texas

ARUN KUMAR AND WANQIU WANG

Climate Prediction Center, NOAA/NWS/NCEP, College Park, Maryland

(Manuscript received 10 November 2012, in final form 8 April 2013)

ABSTRACT

The subsurface ocean temperature response to El Niño–Southern Oscillation (ENSO) is examined based on 31-yr (1981–2011) simulations with the National Centers for Environmental Prediction (NCEP) Climate Forecast System (CFS) coupled model. The model sea surface temperature (SST) in the tropical Pacific is relaxed to observations to ensure realistic ENSO variability in the simulations.

In the tropical Pacific, the subsurface temperature response to the ENSO SST is closely related to the variability of thermocline. The subsurface response is stronger and deeper in the tropical Indian Ocean than in the tropical Atlantic. The analysis at three selected locations reveals that the peak response of the subsurface temperature to ENSO lags the Niño-3.4 SST by 3, 6, and 6 months, respectively, in the southern tropical Indian Ocean, the northern tropical Atlantic, and the North Pacific, where SSTs are also known to be strongly influenced by ENSO. The ENSO-forced temperature anomalies gradually penetrate to the deeper ocean with time in the North Pacific and the tropical Atlantic, but not in the tropical Indian Ocean where the subsurface response at different depths peaks almost at the same time (i.e., at about 3–4 months following ENSO). It is demonstrated that the ENSO-induced surface wind stress plays an important role in determining the time scale and strength of the subsurface temperature response to ENSO in the North Pacific and the northern tropical Atlantic. Additionally, the ENSO-related local surface latent heat flux also contributes to the subsurface response to ENSO in these two regions.

1. Introduction

El Niño–Southern Oscillation (ENSO) is a major source of interannual variability in Earth's climate system. The atmospheric response to ENSO has been extensively studied in the past three decades. The processes involve displacement in the tropical heating associated with ENSO sea surface temperature (SST) anomalies and the resulting atmospheric teleconnections that connect remote atmospheric circulation variability to ENSO (Horel and Wallace 1981; Trenberth et al. 1998). The influence of ENSO, however, is not only confined to the atmospheric variability. The atmospheric teleconnections, and

associated air–sea interactions over other ocean basins, act as a "bridge" linking the variability of SST in global oceans to ENSO (Alexander et al. 2002). It has been shown that ENSO has significant influence on the SST anomalies in the other ocean basins, including the tropical Indian Ocean, tropical Atlantic, and North Pacific (e.g., Huang and Shukla 2007; Klein et al. 1999; Lau and Nath 2001).

Besides the response in SST alone, ENSO also is expected to exert influence on the subsurface ocean temperature and, in turn, might impart a longer time scale memory in remote ocean basins. However, the characteristics of the subsurface ocean temperature response to ENSO have not been assessed in much detail. This is partially due to the lack of subsurface ocean observational data with sufficient temporal and spatial coverage over different water layers in the oceans.

In modeling studies, the ENSO-forced atmospheric variability has been usually assessed with the Atmospheric

Corresponding author address: Dr. Hui Wang, NOAA Climate Prediction Center, 5830 University Research Court, NCWCP, College Park, MD 20740.
E-mail: hui.wang@noaa.gov

Model Intercomparison Project (AMIP) type of experiments in which global SSTs are prescribed as boundary forcing (e.g., Lau 1985; Kumar and Hoerling 1995; Wang and Fu 2000). Following the same paradigm, ENSO-forced subsurface oceanic variability can be assessed with the Coupled Model Intercomparison Project (CMIP) type of simulations (Meehl et al. 2000), in which the atmosphere and ocean are fully coupled. However, unlike the AMIP simulations that can be forced by the observed time-varying SST, and are thus driven by the realistic ENSO variability, the CMIP simulations suffer from biases in the simulated ENSO variability (Guilyardi et al. 2012). This in turn could affect the fidelity of the atmospheric teleconnection and air–sea interactions in the other ocean basins and lead to unrealistic inferences about subsurface ocean responses to ENSO. Further, in the CMIP simulations the evolution of SST related to ENSO is not constrained to follow the observed SST evolution as is the case for the AMIP simulations.

This potential disadvantage of using CMIP configuration to study the subsurface ocean response to ENSO can be avoided by relaxing model SST to the observed values in the tropical Pacific, while the atmosphere and ocean over the rest of the global oceans remain freely coupled. In such an experimental setup, not only is the SST variability in the eastern tropical Pacific realistic and constrained to follow its observed counterpart, but the time evolution of oceanic response in other ocean basins can also be validated against the observational counterpart. Such simulations enable us to characterize various features of the subsurface ocean response to ENSO in a manner similar to what has been done for analyzing the atmospheric response to ENSO variability with the AMIP simulations.

This study aims to characterize the subsurface ocean temperature response to ENSO in different ocean basins in terms of its spatial structure and temporal evolution. The analysis is based on an ensemble of the coupled model simulations where SSTs in the tropical Pacific, by design, are constrained to follow the observed evolution over the 1981–2011 period. The results based on the model simulations are compared with the data from a global ocean data assimilation system. The conceptual and the experimental framework of the analysis are analogous to the analysis of the atmospheric variability forced by ENSO that has been performed in many previous studies with the AMIP simulations. It is expected that our analysis will (i) provide insights into the connections between the variability of the ENSO SST in the tropical Pacific and the variability of subsurface ocean temperature in the other ocean basins and (ii) allow attribution of subsurface oceanic variability in different ocean basins to ENSO. The latter aspect has

been extensively used for attribution of atmospheric variability to ENSO (e.g., Jha and Kumar 2009).

The questions we explore in this study are the following: What are the horizontal and vertical structures of subsurface ocean temperature response to ENSO? What is the typical time scale of SST and subsurface temperature response to ENSO in the tropical Indian Ocean and tropical Atlantic, as well as the North Pacific? How does the time scale of the subsurface ocean response change with depth? What are the mechanisms responsible for different characteristics of subsurface ocean temperature response to ENSO in different ocean basins?

This paper is organized as follows. Section 2 provides a brief description of the model and experimental design. The characteristics of subsurface ocean temperature response to ENSO are examined in section 3, including both spatial structure and temporal evolution. Comparisons between model results and observations are presented with focus on the tropical Indian Ocean, tropical Atlantic, and North Pacific. Mechanisms responsible for different characteristics in different ocean basins are also explored. Conclusions are given in section 4.

2. Data and model simulation design

The observational data used in this study include both weekly and monthly SST, as well as monthly subsurface ocean temperature. The SST dataset is the National Oceanic and Atmospheric Administration (NOAA) Optimum Interpolation SST (OISST) version 2 (Reynolds et al. 2002) on a $1° \times 1°$ (latitude $\times$ longitude) grid. The subsurface ocean temperatures are from the National Centers for Environmental Prediction (NCEP) Global Ocean Data Assimilation System (GODAS; Behringer and Xue 2004) on a $1° \times 2°$ (latitude $\times$ longitude) grid. Both datasets cover a 31-yr period from 1981 to 2011.

The coupled model employed in this study is the early version of the Climate Forecast System (CFS) that was implemented for operational seasonal forecast at NCEP in 2004 (Saha et al. 2006) and was replaced by a new version in 2012 (Saha et al. 2013). In this version of the CFS, the atmospheric, oceanic, and land components of the coupled model are the NCEP Global Forecast System (GFS) version 1 (Moorthi et al. 2001), the Geophysical Fluid Dynamics Laboratory (GFDL) Modular Ocean Model version 3 (MOM3; Pacanowski and Griffies 1998), and the Oregon State University (OSU) land surface model (LSM; Pan and Mahrt 1987), respectively.

The atmospheric GFS has T62 horizontal resolution and 64 vertical levels. The GFDL MOM3 covers global oceans from 74°S to 64°N, with horizontal resolutions of 1° (longitude) by ⅓° (latitude) between 10°S and 10°N,

and increasing to 1° (latitude) poleward of 30°S and 30°N. The MOM3 has 40 layers from 5 m below sea level to 4479 m, with a 10-m resolution in the upper 240 m. The output data from the ocean model were interpolated on the same 1° × 2° (latitude × longitude) grid as GODAS data. The OSU LSM has two soil layers: 0–10 cm and 10–190 cm. More detailed descriptions of the CFS are given in Saha et al. (2006).

To constrain global atmosphere and ocean responses to realistic ENSO variability, tropical Pacific SSTs in the coupled model simulations are relaxed to the observed daily SST. This is done by replacing the model-predicted SST in the tropical Pacific domain (10°S–10°N, 140°E–75°W) with new SST after one-day integrations of the coupled model. The new SST (SST_{NEW}) is a combination of the coupled model predicted SST (SST_{MON3}) and the observed daily SST (SST_{OBS}) interpolated from the weekly OISST based on the following equation:

$$SST_{NEW} = (1 - w)SST_{MOM3} + wSST_{OBS},$$

where w is a weighting coefficient, which is set to ⅓ in the tropical Pacific domain (10°S–10°N, 140°E–75°W) and is linearly reduced to 0 on the border of an extended domain (15°S–15°N, 130°E–65°W). The value of ⅓ for the weighting coefficient, equivalent to nudging the model SST to the observed SST with a restoring time scale of 3.3 days, effectively constrains monthly mean SST_{NEW} in the tropical Pacific to the observations and thus ensures the realistic ENSO variability in the CFS. In the rest of global oceans ($w = 0$), the atmosphere and ocean remain fully coupled. The experimental setup is similar to one used in the analysis by Wang et al. (2012b) and Kumar et al. (2013).

Simulations with such an experimental design are equivalent to the AMIP type of experiments in which SST is prescribed over the tropical Pacific. Elsewhere the simulations are equivalent to the CMIP type in which air–sea interactions are allowed. The model configuration not only eliminates the CFS model bias in simulating the variability of the ENSO SST in the tropical Pacific (Wang et al. 2010) but, more importantly, it also enables us to assess the realism of the subsurface oceanic variability forced by the real ENSO SST through the "atmospheric bridge" (Alexander et al. 2002), against its observational counterpart.

The modified CFS with relaxation of the model predicted SST to the observed SST in the tropical Pacific (TPCF) was integrated over the 31-yr period (1981–2011) with one ocean initial condition but nine different atmospheric initial conditions. The ocean model was initialized with 1 January 1981 condition obtained from GODAS. The atmospheric model was initialized with 28 December 1980–5 January 1981 conditions, each one day apart, obtained from the NCEP–Department of Energy (DOE) Global Reanalysis 2 (R2; Kanamitsu et al. 2002). This procedure results in an ensemble of nine simulations in which the SST variability in equatorial tropical Pacific follows the observed evolution, while SST variability in other ocean basins is a combination of internal variability and variability due to ENSO. Hereafter these simulations are referred to as CFS–TPCF.

Compared to GODAS, the CFS–TPCF runs simulate both the mean state and the variability of subsurface ocean temperature reasonably well in the tropical Indian Ocean and the tropical Pacific, as well as the mean state in the tropical Atlantic (not shown). However, the temperature variability (standard deviation) in the tropical Atlantic near the thermocline is about 20%–40% lower in CFS–TPCF than in GODAS. This set of CFS–TPCF simulations has also been used to study the predictability of seasonal-mean precipitation over the tropical Indian Ocean (Chen et al. 2012).

In this study, the ENSO variability is represented by the variation of the 31-yr monthly time series of the Niño-3.4 index, obtained by averaging SST anomalies in the Niño-3.4 region (5°S–5°N, 120°–170°W). The subsurface response to ENSO is characterized by the correlations between the Niño-3.4 index and subsurface ocean temperature with different lags. The time scale of the ocean temperature response to ENSO is estimated by the lagged months when the lag correlation reaches a maximum. To make a consistent comparison with GODAS, correlations between the Niño-3.4 index and ocean temperature in the CFS–TPCF runs are calculated first for individual members and then are averaged over the nine members.

3. Results

a. Spatial characteristics of ocean temperature response to ENSO

Similar to the analysis of atmospheric variability forced by ENSO in Kumar and Hoerling (1995), a signal-to-noise ratio (SNR) for ocean temperature variability forced by the tropical Pacific SST in the CFS–TPCF runs is calculated at 5-, 55-, and 105-m depths, respectively, and is shown in Fig. 1. The SNR analysis attempts to quantify the temperature variability in other ocean basins that is forced by remote ENSO SST variability relative to local internal variability. As in Kumar and Hoerling (1995), the SNR is defined as the ratio of the variance of ensemble means to the internal variance due to the spread of the ocean temperature among the nine members based on monthly mean data over all the months of the 31 years (1981–2011).
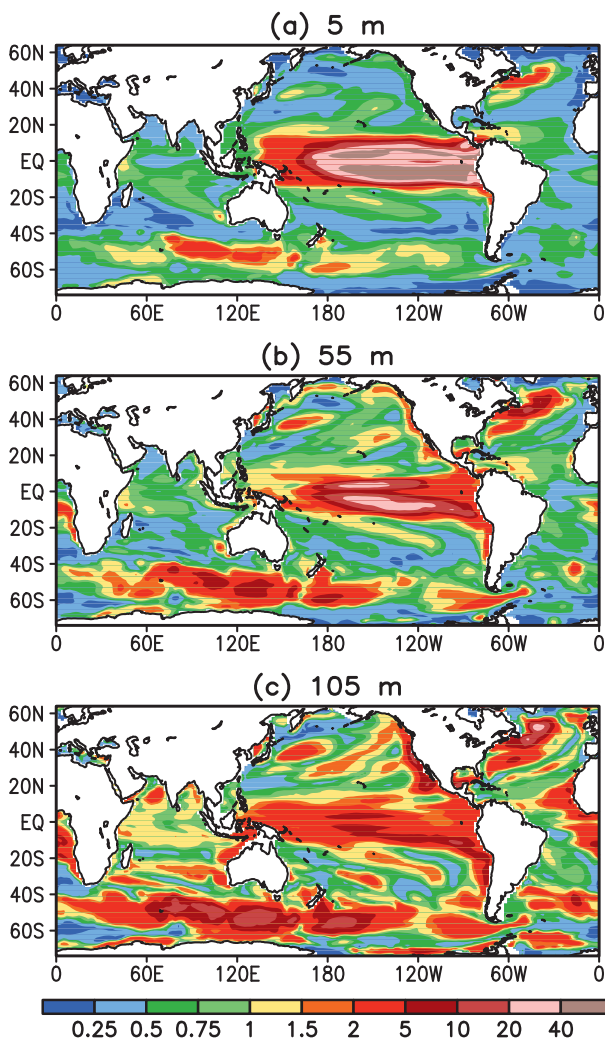
FIG. 1. Signal-to-noise ratio (SNR) for ocean temperature at (a) 5-, (b) 55-, and (c) 105-m depths based on the nine members of 1981–2011 CFS–TPCF runs.

The 5-m depth is in the first layer of the MOM3 ocean model. The ocean temperature at this depth is taken as SST, which is relaxed to the observed SST in the tropical Pacific (10°S–10°N, 140°E–75°W). Consequently, the SNR at the 5-m depth (Fig. 1a) shows very high values (>10) in the eastern and central tropical Pacific as all nine coupled simulations are relaxed to the same observed SSTs. Away from the equatorial tropical Pacific, in the tropical Indian Ocean, tropical Atlantic, and North Pacific, the SNR is generally less than 1. Relatively high values (>0.5) are found in the southern tropical Indian Ocean and northern tropical Atlantic. In the North Pacific, the SNR ranges from 0.25 to 0.75. The ratio is also pronounced in the northwest Atlantic and between 40° and 60°S in the southern oceans.

While the SST variability in the tropical Pacific is specified in the CFS–TPCF runs, subsurface temperature is not and thus has a response to the specified SST. As the depth increases (Figs. 1b,c), the SNR in the eastern and central tropical Pacific decreases. Different from the eastern and central tropical Pacific, the SNR in the western Pacific is greater at 105-m depth than at 55-m depth because the 105-m depth is closer to the thermocline in the western Pacific, which is strongly related to the ENSO SST variability in the eastern Pacific.

Compared to the SNR for SST (Fig. 1a), the SNR for subsurface temperature in the other ocean basins generally increases with depth, partially due to smaller internal variability in deeper oceans. In some regions, such as the eastern tropical Atlantic and southern extratropical oceans, the high SNR at the 105-m depth (Fig. 1c) is primarily due to the initial spinup whereby ocean temperatures from different ensemble members that started from a common initial state from GODAS tend to drift toward the ocean model's mean state in the deeper oceans with a long characteristic time scale (not shown). This feature is different from the analysis of atmospheric variability in the AMIP simulations where, because of the fast adjustment time scale associated with atmospheric variability, the initial spinup toward model climatology is not much of an issue. As will be discussed later, the fact that a high SNR at some locations is not due to ENSO variability can be discerned by comparing the SNR with the ENSO correlation maps for the ocean temperature variability.

How realistic is the spatial pattern of the SNR shown in Fig. 1 and can it be attributed to the specified ENSO variability? Although the SNR (which depends on the availability of the number of model ensemble members) cannot be computed for the observational data, the linear correlation between ENSO SST variability and subsurface temperature variability in the other ocean basins can be compared between model simulations and observations. To assess the fidelity of the link between the variability of the ENSO SST and ocean temperatures, Fig. 2 shows the spatial maps of the correlations between the monthly Niño-3.4 index and ocean temperature at the 5-, 55-, and 105-m depths, respectively, for both the CFS–TPCF runs (left) and GODAS (right) over the 31-yr period. For SST (Fig. 2a), the correlation map displays an El Niño–like pattern in the Pacific, with positive correlations in the eastern and central tropical Pacific and along the west coast of North America, and a "horseshoe" shape of negative correlations in the western tropical and subtropical Pacific. Significant positive correlations are also found in the tropical Indian Ocean and tropical Atlantic. This is mainly true in the model for the Atlantic.
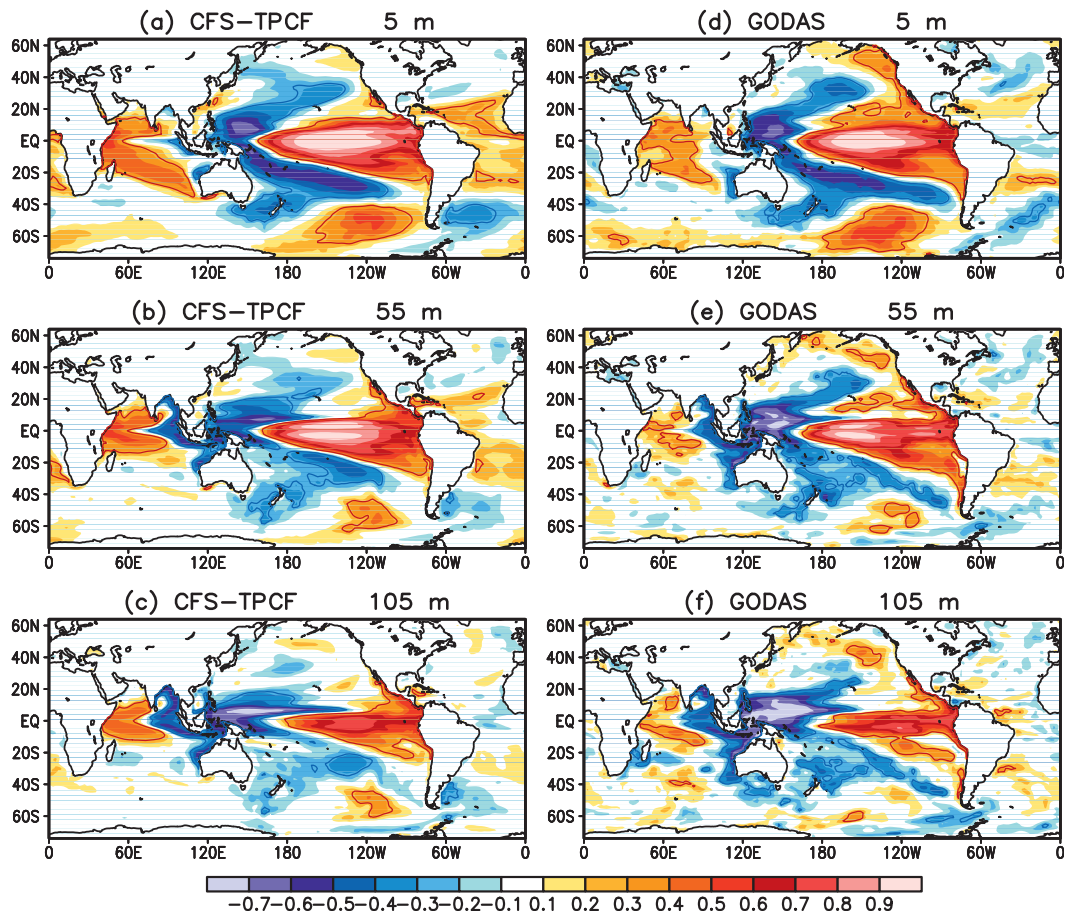
FIG. 2. Correlations between monthly Niño-3.4 index and ocean temperature at (a),(d) 5-, (b),(e) 55-, and (c),(f) 105-m depths in the (left) CFS–TPCF runs and (right) GODAS over the 31-yr period (1981–2011). The values in (a)–(c) are the averages of the correlations for nine individual members. Red (blue) lines indicate the 5% two-tailed significance level for positive (negative) correlations.

The correlation patterns for subsurface temperature (Figs. 2b,c) are similar to that for SST (Fig. 2a). The amplitude of the correlations at 55-m depth is generally greater than that at 105-m depth except for the western tropical Pacific. The correlations are stronger in the tropical Indian Ocean than in the tropical Atlantic. Compared to GODAS (Figs. 2d–f), the correlations in the CFS–TPCF runs are stronger in the tropical Indian Ocean and tropical Atlantic and weaker in the North Pacific. Overall, the relationships between ocean temperature and the Niño-3.4 index in the CFS–TPCF runs, however, are in good agreement with those in GODAS.

A comparison between Figs. 1c and 2c reveals that in some regions where the SNR is large (>2) at the 105-m depth (e.g., the eastern tropical Atlantic and southern midlatitude oceans), the correlation between the ocean temperature and the Niño-3.4 index is small. This indicates that the high SNR may not be attributable to the ENSO variability, at least in the linear sense. The

correlation with the Niño-3.4 index in Fig. 2 can be used to discern the extent that the SNR over a region is due to ENSO variability or to some other factors. Additional analysis (not shown) indicates that in the deeper oceans, and in the regions with small ENSO correlation, the high SNR is due to initial spinup of the model's ocean temperature to its climatology. This spinup being common to all nine simulations, and with the fact that in deeper oceans internal variability is low, gives rise to a common variability resulting in a high SNR despite the fact that the signal is not associated with common ENSO variability. A combination of the spatial distribution of ENSO correlation and the SNR helps us discern the regions of higher SNR that could be attributed to the ENSO variability.

An interesting point to note is that although in our simulations only SSTs in the tropical Pacific are specified, the model is able to generate subsurface variability in the tropical Pacific that has close resemblance to its
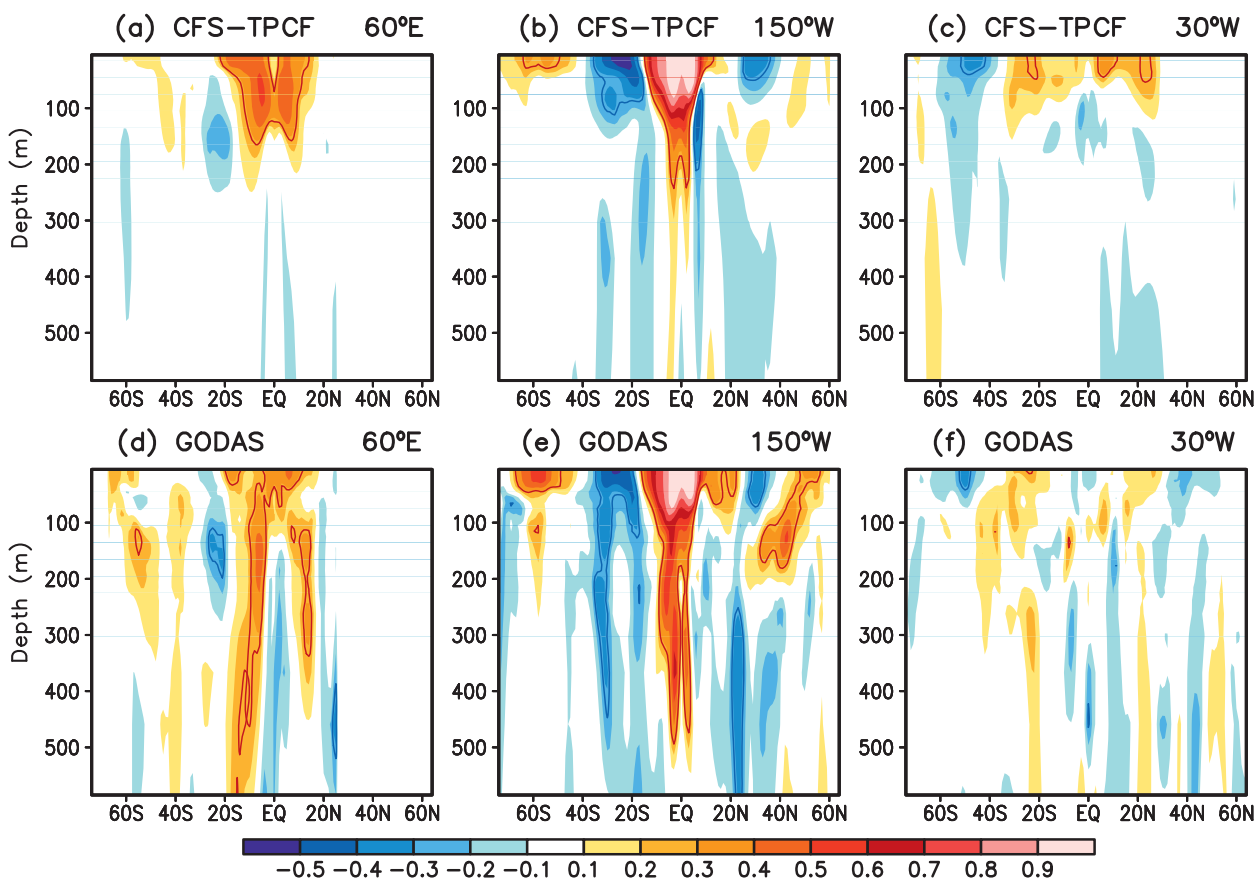
FIG. 3. Latitude–depth cross section of the correlations between monthly Niño-3.4 index and ocean temperature at (a),(d) 60°E, (b),(e) 150°W, and (c),(f) 30°W in the (top) CFS–TPCF runs and (bottom) GODAS over the 31-yr period (1981–2011). Red (blue) lines indicate the 5% two-tailed significance level for positive (negative) correlations.

observational counterpart. This indicates that the specification of SST variability, via its response in surface winds and its subsequent influence on the thermocline variations in the tropical Pacific, is able to simulate realistic subsurface ocean variability. This concept is akin to use of hybrid coupled models where the ocean is coupled to a simple atmosphere in which surface winds are parameterized in terms of SST variability (Zebiak and Cane 1987).

The vertical structure of ocean temperature response to ENSO is examined using vertical cross sections at different longitudes and latitudes. Figure 3 shows such cross sections for the correlations between the Niño-3.4 index and ocean temperature at 60°E (Indian Ocean), 150°W (Pacific), and 30°W (Atlantic) in the CFS–TPCF runs and GODAS, respectively. Along the meridional cross section at the three longitudes, both the SNR (Fig. 1) and the correlation with the Niño-3.4 SST (Fig. 2) are quite representative for the three ocean basins, respectively.

At 60°E (Fig. 3a), the subsurface temperature response to ENSO in the CFS–TPCF runs is confined to the upper ocean above the 200-m depth between 20°S and 20°N, with maximum correlations near the 80-m depth. Consistent with the spatial maps of correlation in Fig. 2, relatively smaller correlation in equatorial latitude is flanked by higher correlations to the north and south. At 150°W (Fig. 3b), the ENSO response in ocean temperature shows a broader meridional extent, with maximum correlations near the ocean surface. The model response in the North and South Pacific is shallower than in the tropics where some weak correlations also exist below the 200-m depth. At 30°W (Fig. 3c), the positive correlations in the tropical Atlantic are weaker and shallower than their counterparts in the tropical Indian Ocean (Fig. 3a), consistent with the results in Figs. 2b and 2c.

Compared to GODAS (Fig. 3, bottom), the subsurface temperature response to ENSO in the CFS–TPCF runs (Fig. 3, top) is stronger in the tropical Indian Ocean above the 150-m depth and weaker below the 150-m depth. In the Pacific basin, the correlations are comparable to each other above the 150-m depth, but slightly weaker below the 150-m depth in the CFS–TPCF runs. In the Atlantic,
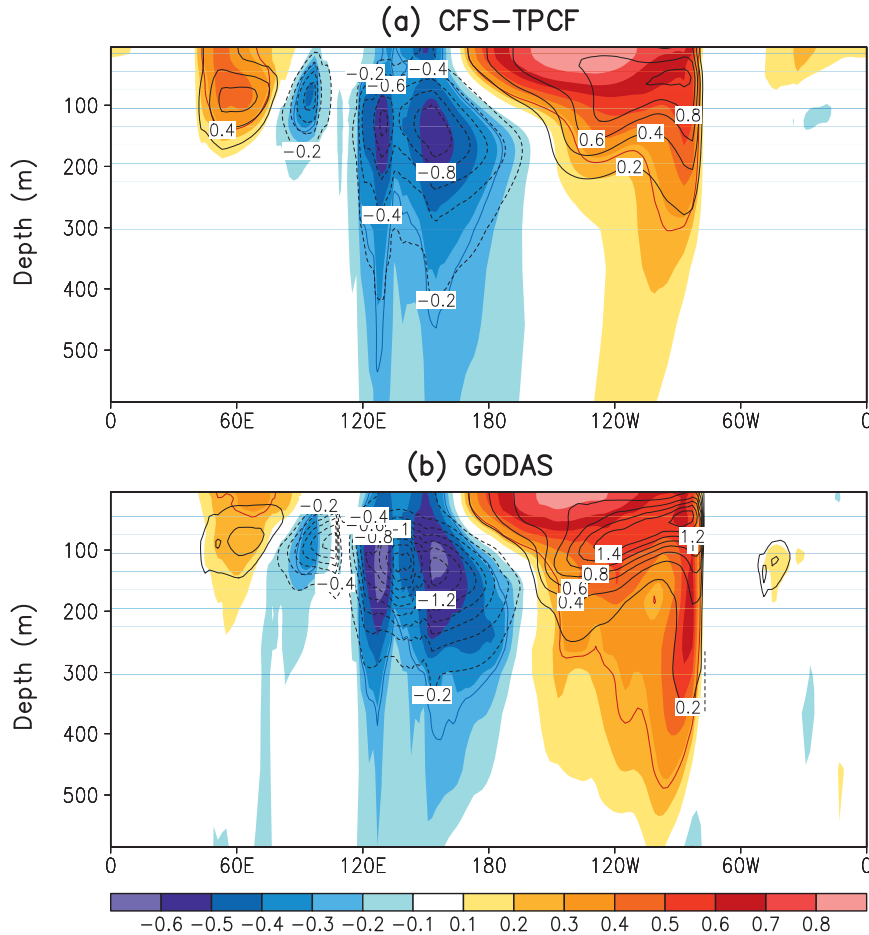
FIG. 4. Longitude–depth cross section of the correlation (shadings) and regression (black contours) coefficients between monthly Niño-3.4 index and ocean temperature in (a) the CFS–TPCF runs and (b) GODAS over the 31-yr period (1981–2011). The values shown are the averages between 10°S and 10°N. Contour interval is $0.2\,\mathrm{K\,K^{-1}}$ with negative contours dashed and zero contours omitted. The regression coefficient is equivalent to the ocean temperature anomaly (K) associated with 1 K of Niño-3.4 SST. Red (blue) lines indicate the 5% two-tailed significance level for positive (negative) correlations.

correlations for GODAS do not have a coherent structure and may point to issues with ocean analysis over this region. For example, it was found that the upper ocean 300-m heat content from 10 operational ocean analyses has much larger uncertainty in the tropical Atlantic than in the other two tropical basins (Xue et al. 2012). In spite of the differences in the deeper oceans, the overall meridional features in correlation patterns in the CFS–TPCF runs agree reasonably well with GODAS in the upper oceans.

The characteristics of ocean temperature response to ENSO in the tropical latitudes alone are examined in Fig. 4, which presents the longitude–depth cross section of the 10°S–10°N averaged correlations (shadings) and regression coefficients (contours) between the Niño-3.4 index and ocean temperature in the CFS–TPCF simulations

(Fig. 4a) and GODAS (Fig. 4b), respectively. The magnitude of the regression coefficients is equivalent to the ocean temperature anomaly (K) associated with 1 K of the Niño-3.4 SST.

In the tropical Pacific, large positive correlations dominate the central and eastern Pacific above the 100-m depth, where the thermocline is shallow, and large negative correlations dominate the western Pacific centered between the 100- and 200-m depths, where the thermocline is deeper. The vertical and zonal structures reflect the subsurface temperature variability along the thermocline during the mature phase of El Niño with positive ocean temperature anomalies in the eastern Pacific and negative in the western Pacific (e.g., Kumar and Hu 2013). A remarkable similarity between Figs. 4a and 4b indicates that both the subsurface temperature

and thermocline responses to the ENSO SST in the tropical Pacific are reproduced well in the model. However, compared to GODAS, the large positive correlations below the 150-m depth in the eastern Pacific near 90°W are underestimated in the CFS–TPCF runs, indicating a possibility for much weaker anomalous downwelling (upwelling) in this region during El Niño (La Niña) in the model when the ENSO SST alone is prescribed. Additionally, the maximums of both positive and negative ocean temperature anomalies associated with 1 K of the Niño-3.4 SST in the CFS–TPCF runs (∼1 K) are smaller than in GODAS (∼1.5 K). This suggests that the ENSO-forced variability only partially accounts for the subsurface temperature variability.

The correlation pattern in the tropical Indian Ocean (Fig. 4a) is characterized by positive correlations in the west above the 200-m depth and negative correlations in the east centered at the 100-m depth. The pattern is similar to that in GODAS (Fig. 4b) and the correlations are slightly stronger in the CFS–TPCF runs. Consistent with the correlation, the warm ocean temperature anomalies (regression coefficients) around 60°E are slightly larger in the CFS–TPCF runs than in GODAS.

In the tropical Atlantic, weak positive correlations are found above the 100-m depth in the CFS–TPCF runs, but no apparent correlations are found in GODAS. In general, the ENSO-related subsurface temperature anomalies are small in the tropical Atlantic. Both Figs. 3 and 4 suggest a stronger and deeper response of the subsurface temperature to the ENSO SST in the tropical Indian Ocean than in the tropical Atlantic. The weak subsurface temperature response to ENSO in the tropical Atlantic may be related to the inconsistent relationship between the Pacific El Niño and the Atlantic Niño found in Chang et al. (2006) and Lübbecke and McPhaden (2012). They argued that the tropical Atlantic SST response to ENSO can be diffused by the local air–sea interaction in the equatorial Atlantic, leading to a weak relationship between the tropical Atlantic SST and ENSO.

b. Temporal characteristics of ocean temperature response to ENSO

The time evolution of ocean temperature response to ENSO is examined based on its correlation with the Niño-3.4 index with different lags. Figure 5 shows the Hovmöller diagram of the correlations between the Niño-3.4 index and the 5-, 55-, and 105-m ocean temperatures at 60°E (Indian Ocean), 150°W (Pacific), and 30°W (Atlantic) in the CFS–TPCF runs and GODAS, respectively, when the ocean temperatures lag the Niño-3.4 index by 0–24 months.

For SST (5-m ocean temperature) in the CFS–TPCF runs, at 150°W (Fig. 5b) between 15°S and 15°N in the tropical Pacific, the lagged correlation varies from positive values during 0- to about 10-month lags to negative values at longer lags. This reflects the ENSO cycle during the 24-month period and the change in ENSO from one phase to the opposite. Between 20° and 40° (latitude) in both the South and North Pacific, the SST responds to ENSO in an opposite way (negatively correlated), consistent with the horseshoe shape of negative correlations in Fig. 2a. Moreover, Fig. 5b indicates that the North Pacific SST responds to ENSO more slowly than the South Pacific SST as the negative correlations reach a peak value at a 1-month lag in the South Pacific but at a 3- or 4-month lag in the North Pacific. This may be because of the seasonality of ENSO SST variability that peaks in boreal winter and its interaction with the seasonality of mixed layer depth, as well as the difference in the amplitude of internal variability in atmospheric forcing between the two hemispheres. As the lag time increases, the negative correlations centered in the subtropical Pacific extend to higher latitudes, suggesting that the impact of ENSO propagates poleward for time scales longer than 6–12 months.

At 60°E (Fig. 5a) in the tropical Indian Ocean, the SST response to ENSO in the CFS–TPCF is in phase with the ENSO SST. The time scale for the positive correlations reaching peak values is about 2–3 months, consistent with the notion of delayed SST response to ENSO in other ocean basins. At 30°W (Fig. 5c) in the tropical Atlantic, the SST response to ENSO is also in phase with the ENSO SST. However, the positive correlations are weaker and the time scale for maximum correlations is about 2 months longer than the SST in the tropical Indian Ocean (Fig. 5a). The response time scale of 4–6 months in the tropical Atlantic is consistent with the finding in Enfield and Mayer (1997) and Hu et al. (2012).

The time evolution of the SST response to ENSO at the selected longitudes in different ocean basins in the CFS–TPCF runs (Figs. 5a–c) has a good resemblance with that in GODAS (Figs. 5d–f). The correlation maps between the Niño-3.4 index and the subsurface temperature at 55-m (Figs. 5g–l) and 105-m (Figs. 5m–r) depths display similar characteristics as the SST (Figs. 5a–f). The correlation patterns for the subsurface temperature in the CFS–TPCF also bear resemblance to their counterpart in GODAS. Over some regions, especially in the tropical Atlantic and North Pacific near 30°N, the maximum correlations for the subsurface temperature lag the maximum correlations for SST. This implies that the impact of ENSO on the subsurface temperatures over these regions is at longer time scales than its impact on SST. In contrast, the subsurface response in the tropical Indian Ocean is more in phase with the surface response. In the central tropical Pacific
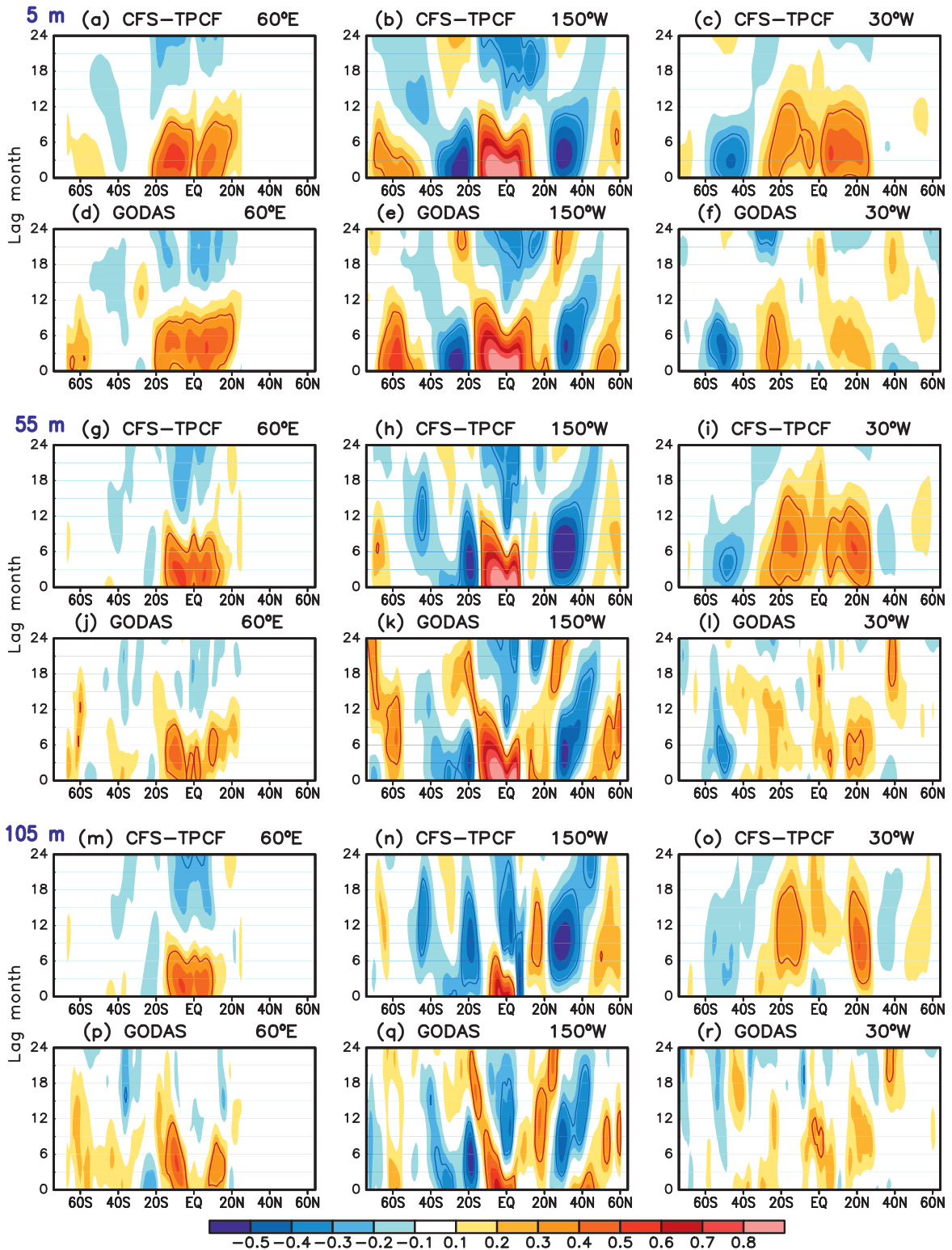
FIG. 5. Hovmöller diagram of the correlations between monthly Niño-3.4 index and the 5-m depth ocean temperature at (a),(d) 60°E, (b),(e) 150°W, and (c),(f) 30°W in (a)–(c) the CFS–TPCF runs and(d)–(f) GODAS over the 31-yr period (1981–2011) when the ocean temperature lags the Niño-3.4 index by 0–24 months, and the corresponding correlations with the (g)–(l) 55-m- and (m)–(r) 105-m-depth ocean temperatures, respectively. Red (blue) lines indicate the 5% two-tailed significance level for positive (negative) correlations.
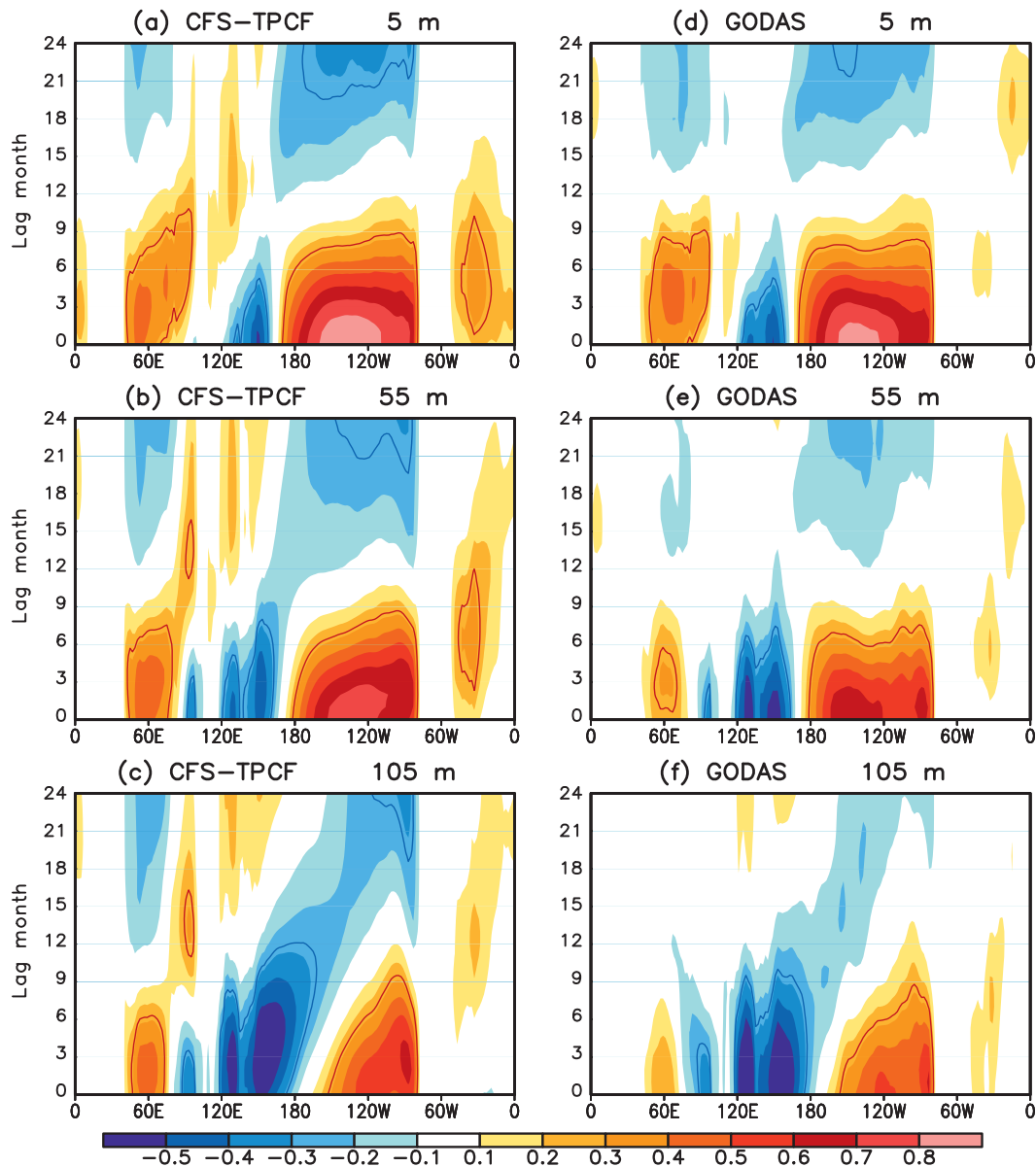
FIG. 6. As in Fig. 5, but for the correlations averaged between 10°S and 10°N with the ocean temperature at (a),(d) 5-, (b),(e) 55-, and (c),(f) 105-m depths in the (left) CFS–TPCF and (right) GODAS.

(150°W), the change in correlation from positive to neg-ative at the 105-m depth (Figs. 5n,q) leads the same change at the 5-m depth (Figs. 5b,e) by 6 months, indicating that the signal of the ENSO phase change appears first in the subsurface.

The subsurface response to ENSO in the tropical oceans is further assessed in Fig. 6, which shows the lagged correlations between ocean temperature and the Niño-3.4 index averaged between 10°S and 10°N. Con-sistent with Figs. 5b and 5e, the lagged correlation pat-tern for SST in the eastern and central Pacific indicates an ENSO phase change in the middle of the 24-month

period in both the CFS–TPCF runs (Fig. 6a) and GODAS (Fig. 6d). The negative correlations for SST in the western tropical Pacific decrease with lag time at the same pace as the positive correlations in the central and eastern Pacific. In the tropical Indian Ocean, the posi-tive correlations with maximums at 3-month lag propa-gate eastward with lag time, which is more apparent in the CFS–TPCF runs (Fig. 6a) than in GODAS (Fig. 6d). The eastward progression of the positive correlations may reflect the ENSO-forced westerly wind anomalies in the western Indian Ocean that project onto strong equatorial westerly currents, known as Wyrtki jets (Wyrtki

1973). Together with the tropical current system on both sides of the equator, including the ubiquitous Rossby waves and Kelvin waves, the westerly wind anomalies generate an anomalous eastward advection in subsequent months, leading to eastward expansion of warm SST anomalies in the following months (Murtugudde and Busalacchi 1999; Alexander et al. 2002). In the tropical Atlantic, the positive correlations for SST are strongest at 30°W with maximums at 4- to 5-month lag in the CFS–TPCF runs (Fig. 6a). They are weaker than those in the tropical Indian Ocean. The tropical Atlantic SST response is stronger in the CFS–TPCF runs than in GODAS (Fig. 6d), consistent with the results in Figs. 2a and 2d.

To some degree, the tropical subsurface ocean temperature responds to ENSO in a similar way to SST (Fig. 6); however, differences in the correlation with the Niño-3.4 index are also apparent between the ocean temperatures at the surface (5-m depth) and the subsurface (55- and 105-m depths) both in the CFS–TPCF (Fig. 6, left column) and GODAS (Fig. 6, right column). Overall, the subsurface temperature response to ENSO in the CFS–TPCF agrees with GODAS better in the tropical Pacific than in the tropical Atlantic and Indian Oceans, presumably due to the relaxation of the model SST to observations in the tropical Pacific. In both the CFS–TPCF and GODAS, the subsurface temperature has a stronger in-phase (out of phase) relationship with ENSO at the 55-m (105 m) depth than at the 105-m (55 m) depth in the eastern and central (western) Pacific, consistent with the vertical structure in Fig. 4. Figure 6 also illustrates that the negative correlations for the subsurface temperature in the central and eastern Pacific at lags longer than 6 months originate from the thermocline response to ENSO in the western Pacific, and are indicative of the response to ENSO-related surface wind that during El Niño (La Niña) leads to an elevated (depressed) thermocline in the western Pacific.

In the tropical Indian Ocean, the positive correlations near 60°E in the CFS–TPCF runs (Fig. 6, left column) display the same lag relationship with ENSO at all three different depths, with peak correlations occurring at the lag time shorter than 6 months. At longer lags, the eastward propagation of the ENSO-related response is evident in both the surface and subsurface. In GODAS (Fig. 6, right column), the same lag relationship with ENSO also exists at the three different depths. However, the eastward propagating feature is not evident.

In the tropical Atlantic, the correlations between the Niño-3.4 index and subsurface temperature are spatially more coherent in the CFS–TPCF than in GODAS. The correlations near 30°W are weaker and lag the Niño-3.4 index longer than those near 60°E (Figs. 6b,c), indicating

that the subsurface temperature response to ENSO is weaker and may have a longer time scale in the tropical Atlantic than in the tropical Indian Ocean.

The subsurface temperature response to ENSO at different depth and lag time is further examined at three specific locations, as shown in Fig. 7, which are selected in the southern tropical Indian Ocean (10°S, 60°E), the North Pacific (30°N, 150°W), and the northern tropical Atlantic (15°N, 30°W). Around the three locations, the SNR is relatively large (Fig. 1) and the correlations of subsurface temperature with the Niño-3.4 index are also large (Figs. 5a–c). The results presented in Fig. 7 are not sensitive to the choice of the exact locations in nearby regions.

In the southern tropical Indian Ocean (Fig. 7a), the subsurface temperature response to ENSO is confined to the upper ocean above the 300-m depth in the CFS–TPCF runs with maximum lagged correlations above the 50-m depth at 3- to 4-month lag. In GODAS (Fig. 7d), the strongest temperature response to ENSO occurs at the 150–300-m depths. The time scale for the maximum correlation at 200-m depth is 6 months. Although the impact of ENSO in the tropical Indian Ocean is shallower and the time scale is shorter in the CFS–TPCF than in GODAS, the sign of the response and its transition from positive to negative as lead time increases are nonetheless reasonably represented.

In the North Pacific (Fig. 7b), the subsurface response to ENSO penetrates progressively deeper with lag time. The strongest response is above 100-m depth at 4- to 10-month lags in the CFS–TPCF runs. The impact of ENSO can reach 200-m depth at 15- to 24-month lags. The lagged correlations in GODAS (Fig. 7e) show similar features above the 200-m depth. In summer months, the ocean mixed layer depth is generally less than 25 m in the North Pacific (e.g., Wang et al. 2012a). The penetration of the ENSO signal into the deeper ocean may reinforce the reemergence mechanism (Alexander et al. 1999) and help rebuild North Pacific SST anomalies on decadal time scales. It has been demonstrated in Wang et al. (2012b) that ENSO variability indeed enhances the amplitude of Pacific decadal oscillation at decadal time scales.

In the northern tropical Atlantic (Fig. 7c), the ocean temperature response to ENSO in the CFS–TPCF runs changes with depth and lag month in a way similar to that in the North Pacific (Fig. 7b), although the sign of the lagged correlations is opposite at these two locations. The time scale for maximum lagged correlations is also similar to that in the North Pacific at 4- to 10-month lags, longer than that in the tropical Indian Ocean (Fig. 7a). However, the subsurface temperature response in the tropical Atlantic is above the 150-m depth, shallower
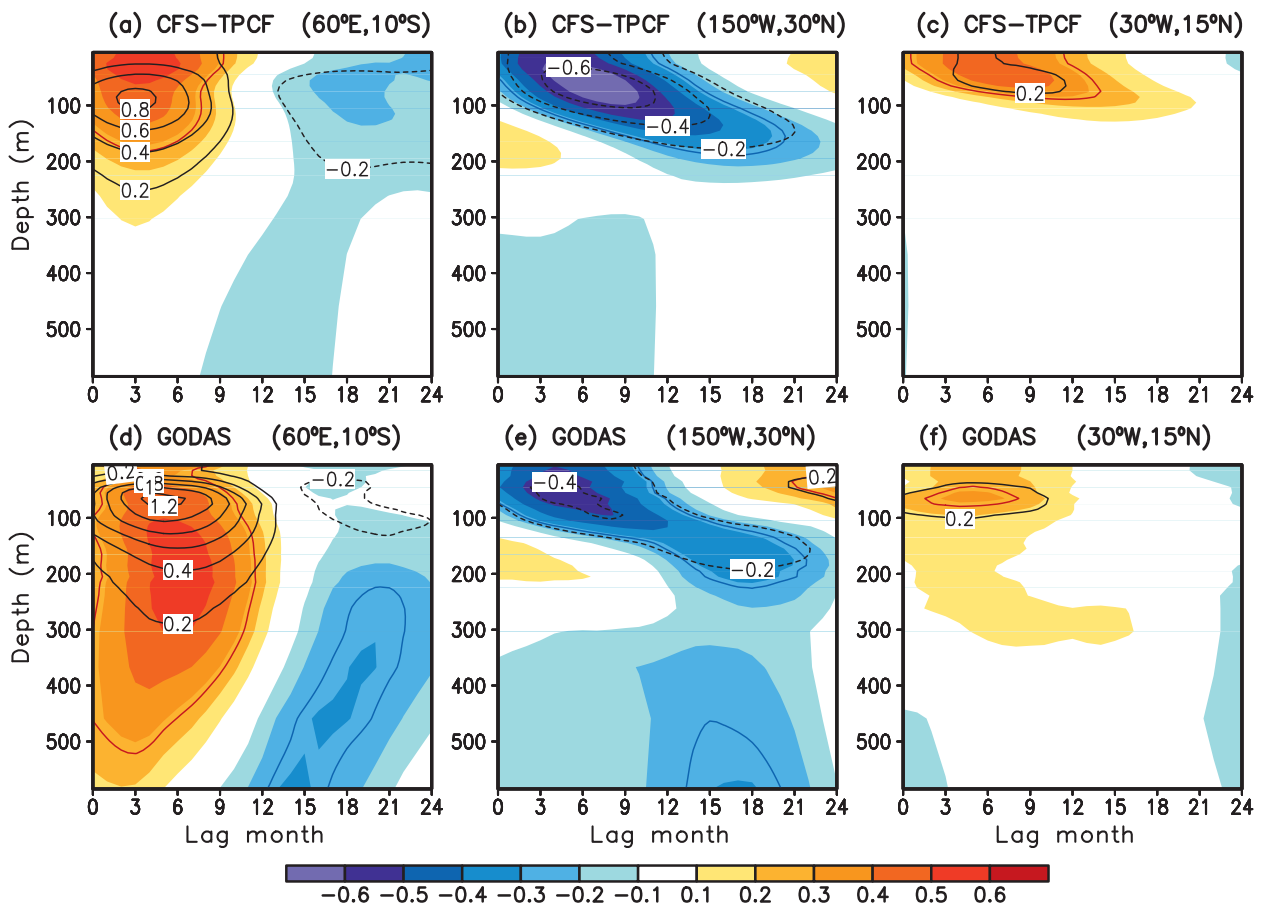
FIG. 7. Lag correlation (shadings) and regression coefficients (black contours) between monthly Niño-3.4 index and ocean temperature at (a),(d) 10°S, 60°E; (b),(e) 30°N, 150°W; and (c),(f) 15°N, 30°W in the (top) CFS–TPCF runs and (bottom) GODAS over the 31-yr period (1981–2011) when the ocean temperature lags the Niño-3.4 index by 0–24 months. The contour interval and red and blue lines are same as in Fig. 4.

than the other two locations. In GODAS (Fig. 7f), the lagged correlations are weaker than those in the CFS–TPCF runs.

The ocean temperature anomalies at the three locations are also plotted in Fig. 7, obtained based on the lagged linear regression of ocean temperature anomalies against the Niño-3.4 index for individual CFS–TPCF runs and then averaged over the nine members, as well as for GODAS. The changes in temperature anomalies with depth are similar to the corresponding lagged correlation patterns and display the same temporal characteristics in response to ENSO. Associated with 1 K of the Niño-3.4 SST, the ocean temperature anomaly in the CFS–TPCF (GODAS) reaches the peak values of 0.8 (1.2) K at month 3 (4) in the tropical Indian Ocean, −0.6 (−0.4) K at month 6 (5) in the North Pacific, and 0.2 (0.2) K at month 6 (5) in the tropical Atlantic.

One of the most striking features displayed in Fig. 7 is the penetration of the ENSO-forced ocean temperature

anomalies to the deeper layers with time in the North Pacific and the tropical Atlantic in the CFS–TPCF runs (Figs. 7b,c). In contrast, temperature anomalies at all depths reach the peak values at the same 3-month lag in the tropical Indian Ocean (Fig. 7a). Similar features are also observed in GODAS (Figs. 7d–f). Additionally, the results presented in Figs. 5–7 consistently suggest that the subsurface temperature response to ENSO is weaker and the response time scale is longer in the tropical Atlantic than in the tropical Indian Ocean.

c. Possible mechanisms

There are several mechanisms that may control or influence the subsurface temperature response to ENSO, leading to the differences in response over different ocean basins, such as the mean state of ocean, ocean mixed layer depth, surface wind stress, and surface heat fluxes. The forcing mechanisms of remote SST response to ENSO identified in previous studies might also explain the

subsurface temperature response to ENSO. For example, Zhang et al. (1996) and Klein et al. (1999) show the importance of shortwave radiation anomalies associated with decreasing cloudiness during El Niño in warming SSTs in the tropical Atlantic and the tropical Indian Ocean. Chiang and Sobel (2002) and Chiang and Lintner (2005) emphasize the mechanisms of the tropical tropospheric temperature warming caused by El Niño subsequently inducing changes in surface latent heat flux for the remote tropical SST response to ENSO. In this section we discuss whether similar mechanisms may operate in the subsurface temperature response to ENSO based on the analysis of the CFS–TPCF runs.

The mean state of the oceans is examined first. Figure 8 shows the 31-yr climatological annual mean ocean temperature at the equator from the nine-member average of the CFS–TPCF runs and GODAS, respectively, as well as the vertical profile of ocean temperature at the three locations discussed in Fig. 7: 10°S, 60°E; 30°N, 150°W; and 15°N, 30°W. In the equatorial Pacific, the 293-K (~20°C) isotherm (green line in Figs. 8a and 8b) is a good approximation of the thermocline, which is shallow in the eastern Pacific and deep in the west. The east–west structure of large positive and negative temperature anomalies in the Pacific sector (Fig. 4) suggests that the strong response to the ENSO SST in the tropical Pacific occurs at the depths along the thermocline and is thus closely related to the variation of the thermocline.

In the tropical Indian Ocean and the tropical Atlantic, the response to ENSO (Fig. 4) is shallower and seems to be less related to the thermocline variability. In the tropical Atlantic, for instance, it has been hypothesized that ENSO exerts its influence via modifying local trade wind and altering wind–evaporation–SST feedback, leading to a shallow response of ocean temperature to ENSO (Hu et al. 2011). The vertical profile of ocean temperature at the three specific locations also indicates that the depths of the upper ocean mixed layer are close to each other (Figs. 8c–e) and may not contribute to the differences in the vertical scale of the ENSO response. This is confirmed by the 31-yr climatological annual mean ocean mixed layer depth (not shown), estimated as the depth at which the temperature change from the ocean surface is 0.5°C (Monterey and Levitus 1997). At the three locations, the mixed layer depths are 57, 57, and 54 m in the CFS–TPCF runs and 39, 56, and 46 m in GODAS.

To further analyze mechanisms leading to the subsurface ocean temperature response to ENSO, Fig. 9 shows the correlations between the Niño-3.4 index and the surface fluxes in the CFS–TPCF runs, including zonal wind stress (or zonal momentum flux, UFLX), downward shortwave radiation flux (DSWRF; downward flux >0),

and latent heat flux (LHTFL; upward flux >0), for surface fluxes lagging the Niño-3.4 index by 3 (left column) and 6 (right column) months, respectively. For the surface zonal wind stress at the 3-month lag (Fig. 9a), correlations exceeding the 5% significance level are found in the tropical Indian Ocean, the North Pacific, and the northern tropical Atlantic where the three locations are selected for the analysis presented in Fig. 7. At the 6-month lag (Fig. 9d), the significant correlations still exist in the North Pacific and the northern tropical Atlantic but are no longer found over the western tropical Indian Ocean. The results suggest that the ENSO-forced surface wind stress anomalies, through the atmospheric teleconnection, are more persistent in the North Pacific and the tropical Atlantic than in the tropical Indian Ocean. The wind stress over the southern tropical Indian Ocean, which has a correlation with the Niño-3.4 index (Fig. 9a), can explain the thermocline variability as in Xie et al. (2002).

For the downward shortwave radiation flux (Figs. 9b,e), there are less significant correlations with ENSO in the areas surrounding the three locations. Over the tropical Pacific, negative correlations for the downward shortwave flux signify a negative feedback to ENSO SSTs noted in earlier studies (e.g., Kumar and Hu 2012). Some correlations between the Niño-3.4 index and surface latent heat flux (Figs. 9c,f) are found in a small area around 150°W in the North Pacific and a zone between 10° and 20°N in the northern tropical Atlantic at the 3-month lag, but neither in the tropical Indian Ocean near 60°E nor at the 6-month lag. This indicates that the ENSO-related latent heat flux in the North Pacific and the northern tropical Atlantic does not last as long as the ENSO-forced surface wind stress.

Given the teleconnections between ENSO and the surface fluxes in the remote oceans (Fig. 9), how the local surface fluxes may drive the subsurface temperature anomalies is further explored. Figure 10 shows the correlation between local surface fluxes and lagged ocean temperature at the same three selected locations as in Fig. 7, as a function of depth and lag time. Similar to the correlation with the Niño-3.4 index (Figs. 7b,c), the correlation of subsurface temperature with local surface wind stress also penetrates into the deeper ocean in the North Pacific (Fig. 10b) and the northern tropical Atlantic (Fig. 10c). The similarity suggests that through the atmospheric teleconnection, the ENSO-induced remote surface wind stress anomalies over these two regions (Figs. 9a,b), in turn, drive the subsurface temperature anomalies. We speculate that the downward penetration of the ENSO signal (Figs. 7b,c) is likely due to upper ocean mixing processes. In contrast, the surface wind stress may not be responsible for the subsurface temperature
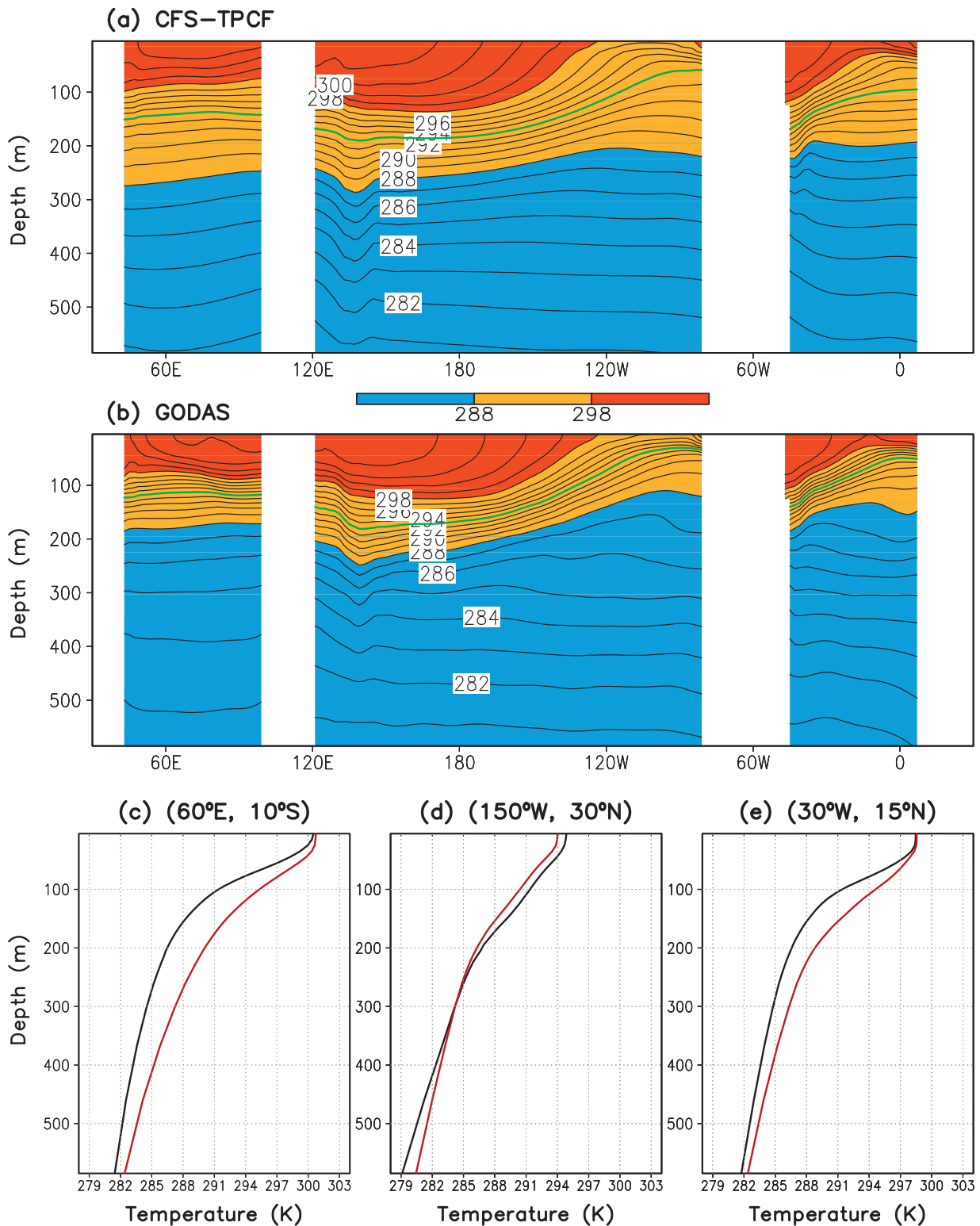
FIG. 8. Climatological annual mean ocean temperature (K) at the equator from (a) the nine-member average of the CFS–TPCF runs and (b) GODAS, and vertical profile of ocean temperature at (c) 10°S, 60°E; (d) 30°N, 150°W; and (e) 15°N, 30°W from the nine-member average of the CFS–TPCF runs (red) and GODAS (black). The green line in (a) and (b) is the 293-K (~20°C) isotherm.
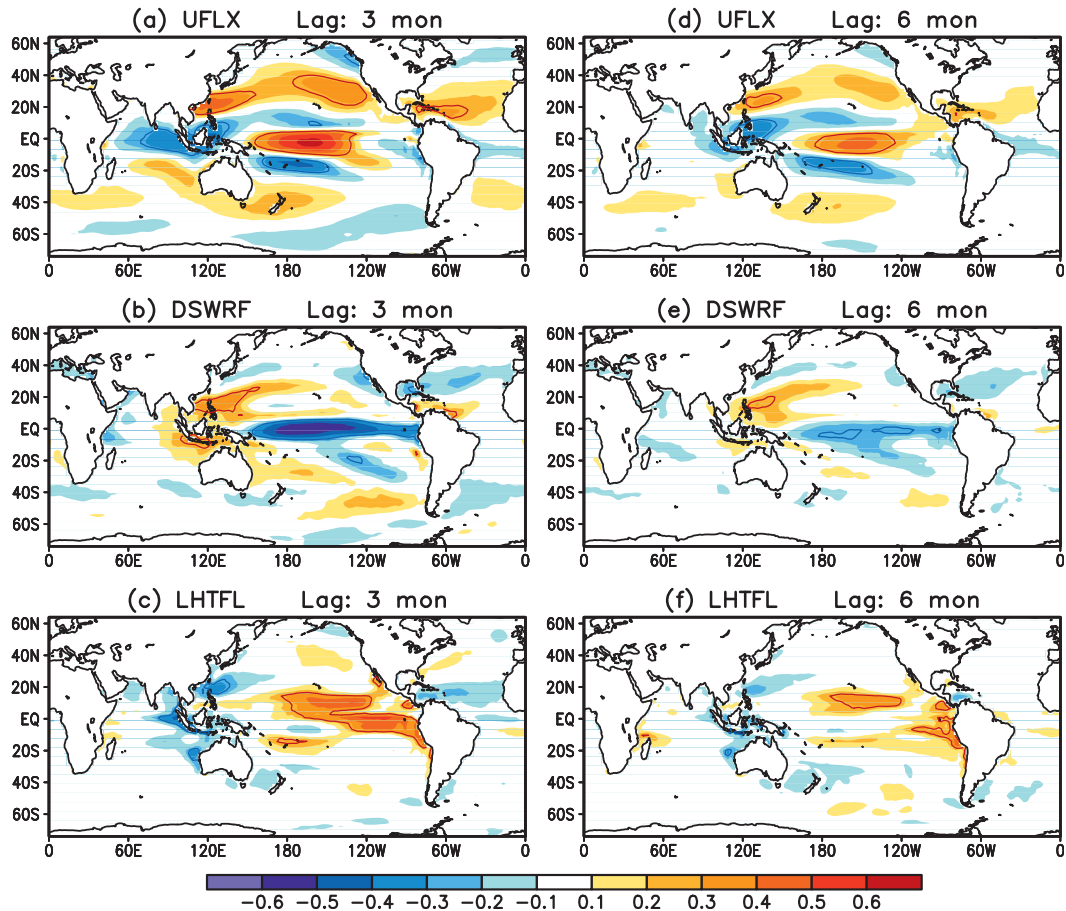
FIG. 9. Correlations between monthly Niño-3.4 index and (a),(d) surface zonal wind stress (UFLX), (b),(e) surface downward shortwave radiation flux (DSWRF), and (c),(f) surface latent heat flux (LHTFL) from the CFS–TPCF runs over the 31-yr period (1981–2011) for the surface fluxes lagging the Niño-3.4 index by (left) 3 and (right) 6 months, respectively. The values shown are the averages of the correlations for nine individual members. Red (blue) lines indicate the 5% two-tailed significance level for positive (negative) correlations.

response to ENSO in the southern tropical Indian Ocean (Fig. 10a). The time scale of the subsurface response to local surface wind stress (Figs. 10b,c), defined as the lagged month for maximum correlations, is shorter than the subsurface response to ENSO (Figs. 7b,c) because there is a delayed response to ENSO for the local surface wind stress (Figs. 9a,b).

The subsurface temperatures at the three locations show no significant correlations with local shortwave radiation flux (Figs. 10d–f). Away from the ocean surface, there are positive correlations with latent heat flux (Figs. 10g–i). These positive correlations also seem to exist when the ocean temperature leads latent heat flux. Near the ocean surface, there are negative correlations when the ocean temperature lags latent heat flux, indicating the subsurface response to local latent heat flux. The lagged relationship between ENSO and latent heat flux (Fig. 9c) and that between local latent heat flux and

subsurface temperature (Figs. 10h,i) suggest a possible mechanism of the subsurface response to ENSO through surface latent heat flux in the North Pacific and the northern tropical Atlantic. Based on the signs of the correlations in Figs. 9c, 10h, and 10i, the ENSO-induced latent heat flux cools the near-surface temperature at (30°N, 150°W) and warms the subsurface temperature at (15°N, 30°W). Compared to the subsurface response to surface wind stress (Figs. 10b,c), the response to latent heat flux is confined more to the upper oceans.

To understand the different response time scales at the different locations, the amplitude of surface wind stress anomaly as a function of lagged month is plotted in Fig. 10j for 30°N, 150°W and 15°N, 30°W, obtained with the lagged linear regression versus the Niño-3.4 index. The amplitude of the anomalies displays similar behavior in the North Pacific (blue line) and tropical Atlantic (red line) with a peak at month 3 and then decays
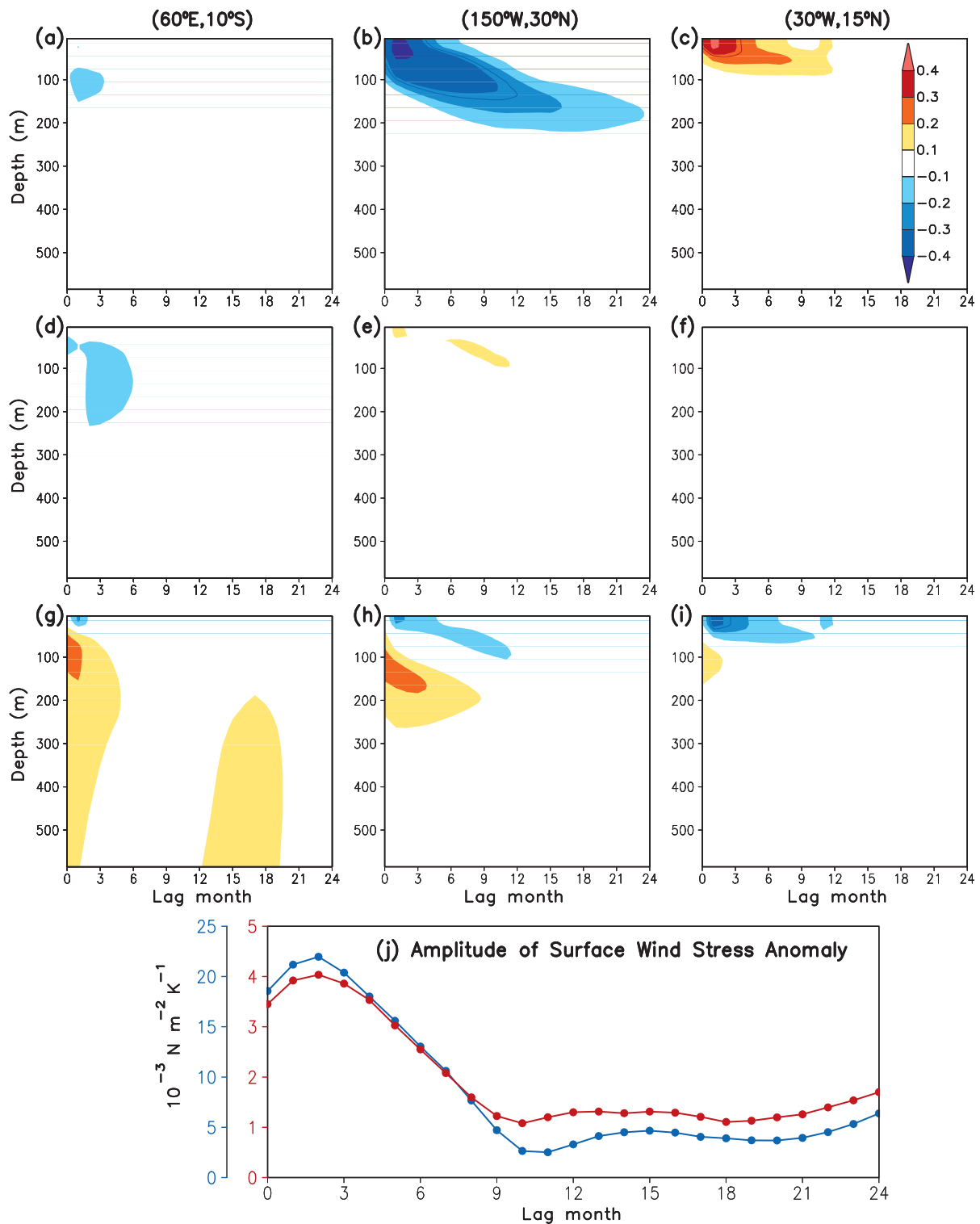
FIG. 10. Lag correlations between ocean temperature and local (a)–(c) zonal wind stress, (d)–(f) downward shortwave radiation flux, and (g)–(i) latent heat flux, respectively, in the CFS–TPCF runs over the 31-yr period (1981–2011) for the ocean temperature lagging the surface fluxes by 0–24 months, at (left) 10°S, 60°E; (center) 30°N, 150°W; and (right) 15°N, 30°W. Red (blue) lines indicate the 5% two-tailed significance level for positive (negative) correlations. (j) The amplitude of surface wind stress anomalies $(10^{-3} \, \mathrm{N \, m^{-2} \, K^{-1}})$ at 30°N, 150°W (blue) and 15°N, 30°W (red) obtained based on lagged linear regressions against the Niño-3.4 index for individual CFS–TPCF runs and then averaged over the nine members, with the surface wind stress lagging the Niño-3.4 index by 0–24 months. The magnitudes correspond to the wind stress anomalies associated with 1 K of Niño-3.4 SST.

with an *e*-folding time of 6 and 5 months, respectively, consistent with the response time scale at the two locations (Figs. 7b,c). This suggests that the response time scale strongly depends on how persistent the surface forcing in response to ENSO is. The peak of the subsurface temperature anomalies lags the peak of the wind stress (Figs. 7b,c), indicating slower oceanic processes involved as the ENSO-forced anomalies propagate downward. The wind stress anomaly is much stronger in the North Pacific than in the northern tropical Atlantic (Fig. 10j), consistent with the relatively large subsurface temperature anomalies in the North Pacific (Fig. 7b) and smaller anomalies in the tropical Atlantic (Fig. 7c).

There are no clear indications in Figs. 9 and 10 that the ENSO-forced local surface flux anomalies are responsible for the strong subsurface temperature response to ENSO in the southern tropical Indian Ocean (Fig. 7a). This is consistent with the finding of Klein et al. (1999) that the ENSO-induced SST warming in the tropical southwest Indian Ocean cannot be explained by surface fluxes. Previous studies (e.g., Xie et al. 2002; Schott et al. 2009) have shown that both SST and subsurface temperature in the western Indian Ocean near 10°S correlate highly with the local thermocline depth variations, suggesting a strong control of SST response, as well as the subsurface response, to ENSO by nonlocal ocean dynamical adjustment (e.g., westward propagating oceanic Rossby waves). Additionally, ENSO has a strong seasonality, which peaks in winter; and so does the response to ENSO in the tropical Indian Ocean, which is most likely significant in the following summer (e.g., Xie et al. 2009). The use of data from all 12 calendar months in the present study could degrade the signals of both the ENSO-induced forcing and the remote subsurface response. Therefore, in addition to the analysis of the surface fluxes, more detailed diagnosis of the CFS–TPCF runs is required to understand the dynamics of the tropical Indian Ocean and its impact on the subsurface response to ENSO.

4. Summary and discussion

The characteristics of the subsurface ocean temperature response to ENSO were documented in this study with the CFS coupled model simulations and a unique experimental setup with the relaxation of model SST to the observations in the tropical Pacific. The methodology used to analyze the component of ENSO response in different ocean basins parallels the use of ensemble of AMIP simulations to analyze the atmospheric circulation response to ENSO in numerous previous studies. Here our emphases were placed on the spatial characteristics of the subsurface temperature response, including both the

horizontal and vertical structures, as well as the associated temporal evolution. The results based on the CFS–TPCF runs were compared to the similar analysis with GODAS data.

The relationships between subsurface temperature and the Niño-3.4 index in the CFS–TPCF runs are overall in good agreement with those in GODAS both horizontally and vertically. In the tropical Pacific, the subsurface temperature response to ENSO is closely related to the variability of the thermocline. The subsurface response to ENSO is stronger and deeper in the tropical Indian Ocean than in the tropical Atlantic.

We also demonstrated that the SST response to ENSO has different time scales in different ocean basins. The time scale of peak response is relatively short (2–3 months) in the tropical Indian Ocean and relatively long (3–6 months) in the tropical Atlantic and the North Pacific. The impact of ENSO on the subsurface temperature is at longer time scales than its impact on SST. It is also found that the subsurface temperature response to ENSO has different temporal characteristics in different ocean basins. The analysis at three selected locations reveals that the peak response of the subsurface temperature to ENSO lags the Niño-3.4 SST by 3, 6, and 6 months, respectively, in the southern tropical Indian Ocean, the northern tropical Atlantic, and the North Pacific. The ENSO-forced temperature anomalies penetrate gradually to the deeper oceans with time in the North Pacific and the tropical Atlantic, but not in the tropical Indian Ocean.

The analysis further suggests that the ENSO-induced surface wind stress plays an important role in determining the time scale and strength of the subsurface temperature response to ENSO in the North Pacific and the northern tropical Atlantic. In addition, the ENSO-related local surface latent heat flux also contributes to the subsurface response to ENSO in these two regions, which is confined to the upper ocean with shorter time scales.

The results presented and the experimental setup used in this study may help us understand the attributions for SST anomalies in the other ocean basins and their link to the ENSO variability. As an example for the attribution of SST anomalies in other ocean basins, Fig. 11 shows the Hovmöller diagram of SST anomalies averaged between 10°S and 10°N in the global tropics from January 2009 to December 2011 based on the OISST and the CFS–TPCF runs, respectively. Following the 2009/10 El Niño, warm SST anomalies were observed in both the tropical Indian Ocean and tropical Atlantic (Fig. 11a). The peak warm SST anomalies in the western Indian Ocean lagged the peak El Niño SST by 2–3 months, while the warm SST in the Atlantic lagged by 3–6 months. These characteristics are well reproduced in the CFS–TPCF runs (Fig. 11b),
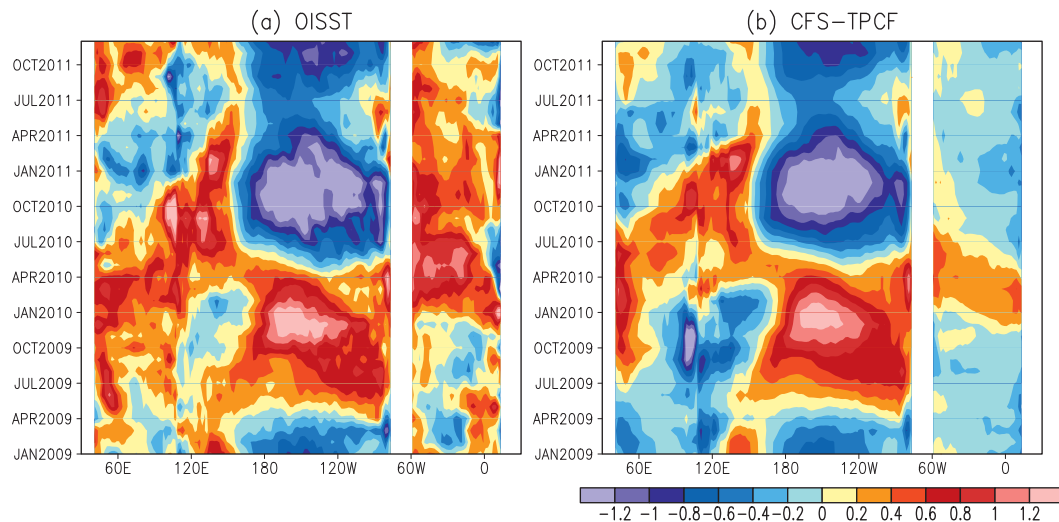
FIG. 11. Hovmöller diagram of monthly SST anomalies (K) averaged between 10°S and 10°N from January 2009 to December 2011 for (a) OISST and (b) the nine-member ensemble mean of the CFS–TPCF runs.

indicating the role of tropical ENSO variability in the evolution of SST anomalies in the Indian and Atlantic Oceans. Moreover, the eastward propagation of the warm SST anomalies in the tropical Indian Ocean is also depicted in Fig. 11b, consistent with the lagged correlation in Fig. 6a. The CFS–TPCF runs (Fig. 11b) further suggest that the warm SST anomalies in the tropical Atlantic after July 2010 (Fig. 11a) might not be forced by the 2009/10 El Niño and might have their origins from local air–sea interactions (e.g., Hu et al. 2011).

There are several related aspects that need to be investigated in the future work. While the annual mean climatology of the mixed layer depth is more or less the same at the three selected locations analyzed, the seasonal variation of the mean mixed layer depth can be very different and may affect the subsurface temperature response to ENSO in different ocean basins. The seasonality of the oceanic response to ENSO should also be considered. It is still not clear why the temperature anomalies peak at month 3 at all different depths in the tropical Indian Ocean (Fig. 7a) and why the vertical structures are different between the CFS–TPCF runs and GODAS (Figs. 7a,d). The local SST variability, such as the Indian Ocean dipole (Saji et al. 1999) and tropical Atlantic variability (e.g., Enfield and Mayer 1997), and the influences of the other ocean basins on the tropical Pacific are not considered in the analysis. They may partially account for the difference between the CFS–TPCF runs and GODAS. Further analysis of the CFS–TPCF runs and observations is required to understand the feedbacks of the different response time scale to local air–sea interactions and their impacts on regional climate, such as the Indian summer monsoon, Atlantic

hurricanes, and the reemergence of North Pacific SST anomaly. In addition to the surface fluxes, thermal advection and the heat budget may also play roles in determining the response time scale. Finally, the results presented in this paper are based on one particular coupled model and need to be confirmed based on other systems.

REFERENCES

Alexander, M. A., C. Deser, and M. S. Timlin, 1999: The reemergence of SST anomalies in the North Pacific Ocean. *J. Climate,* **12,** 2419–2433.

——, I. Bladé, M. Newman, J. R. Lanzante, N.-C. Lau, and J. D. Scott, 2002: The atmospheric bridge: The influence of ENSO teleconnections on air–sea interaction over the global oceans. *J. Climate,* **15,** 2205–2231.

Behringer, D. W., and Y. Xue, 2004: Evaluation of the global ocean data assimilation system at NCEP: The Pacific Ocean. Preprints, *Eighth Symp. on Integrated Observing and Assimilation Systems for Atmosphere, Oceans, and Land Surface,* Seattle, WA, Amer. Meteor. Soc., 2.3. [Available online at http://ams.confex.com/ams/84Annual/techprogram/paper_70720.htm.]

Chang, P., Y. Fang, R. Saravanan, L. Ji, and H. Seidel, 2006: The cause of the fragile relationship between the Pacific El Niño and the Atlantic Niño. *Nature,* **443,** 324–328.

Chen, M., W. Wang, A. Kumar, H. Wang, and B. Jha, 2012: Ocean surface impacts on the seasonal-mean precipitation over the tropical Indian Ocean. *J. Climate,* **25,** 3566–3582.

Chiang, J. C. H., and A. H. Sobel, 2002: Tropical tropospheric temperature variations caused by ENSO and their influence on the remote tropical climate. *J. Climate,* **15,** 2616–2631.

——, and B. R. Lintner, 2005: Mechanisms of remote tropical surface warming during El Niño. *J. Climate,* **18,** 4130–4149.

Enfield, D. B., and D. A. Mayer, 1997: Tropical Atlantic sea surface temperature variability and its relation to El Niño–Southern Oscillation. *J. Geophys. Res.,* **102,** 929–945.

Guilyardi, E., W. Cai, M. Collins, A. Fedorov, F.-F. Jin, A. Kumar, D.-Z. Sun, and A. Wittenberg, 2012: New strategies for evaluating ENSO processes in climate models. *Bull. Amer. Meteor. Soc.,* **93,** 235–238.

Horel, J. D., and J. M. Wallace, 1981: Planetary-scale atmospheric phenomena associated with the Southern Oscillation. *Mon. Wea. Rev.,* **109,** 813–829.

Hu, Z.-Z., A. Kumar, B. Huang, Y. Xue, W. Wang, and B. Jha, 2011: Persistent atmospheric and oceanic anomalies in the North Atlantic from summer 2009 to summer 2010. *J. Climate,* **24,** 5812–5830.

——, ——, B. Jha, and B. Huang, 2012: An analysis of forced and internal variability in a warmer climate in CCSM3. *J. Climate,* **25,** 2356–2373.

Huang, B., and J. Shukla, 2007: Mechanisms for the interannual variability in the tropical Indian Ocean. Part I: The role of remote forcing from the tropical Pacific. *J. Climate,* **20,** 2917–2936.

Jha, B., and A. Kumar, 2009: A comparison of the atmospheric response to ENSO in coupled and uncoupled model simulations. *Mon. Wea. Rev.,* **137,** 479–487.

Kanamitsu, M., W. Ebisuzaki, J. Woollen, S.-K. Yang, J. J. Hnilo, M. Fiorino, and G. L. Potter, 2002: NCEP–DOE AMIP-II Reanalysis (R-2). *Bull. Amer. Meteor. Soc.,* **83,** 1631–1643.

Klein, S. A., B. J. Soden, and N.-C. Lau, 1999: Remote sea surface temperature variations during ENSO: Evidence for a tropical atmospheric bridge. *J. Climate,* **12,** 917–932.

Kumar, A., and M. P. Hoerling, 1995: Prospects and limitations of seasonal atmospheric GCM predictions. *Bull. Amer. Meteor. Soc.,* **76,** 335–345.

——, and Z.-Z. Hu, 2012: Uncertainty in ocean–atmosphere feedbacks associated with ENSO in the reanalysis products. *Climate Dyn.,* **39,** 575–588.

——, and ——, 2013: Interannual and interdecadal variability of ocean temperature along the equatorial Pacific in conjunction with ENSO. *Climate Dyn.,* doi:10.1007/s00382-013-1721-0, in press.

——, H. Wang, W. Wang, Y. Xue, and Z.-Z. Hu, 2013: Does knowing the oceanic PDO phase help predict the atmospheric anomalies in subsequent months? *J. Climate,* **26,** 1268–1285.

Lau, N.-C., 1985: Modeling the seasonal dependence of the atmospheric response to observed El Niños in 1962–76. *Mon. Wea. Rev.,* **113,** 1970–1996.

——, and M. J. Nath, 2001: Impact of ENSO on SST variability in the North Pacific and North Atlantic: Seasonal dependence and role of extratropical sea–air coupling. *J. Climate,* **14,** 2846–2866.

Lübbecke, J. F., and M. J. McPhaden, 2012: On the inconsistent relationship between Pacific and Atlantic Niños. *J. Climate,* **25,** 4294–4303.

Meehl, G. A., G. J. Boer, C. Covey, M. Latif, and R. J. Stouffer, 2000: The Coupled Model Intercomparison Project (CMIP). *Bull. Amer. Meteor. Soc.,* **81,** 313–318.

Monterey, G. I., and S. Levitus, 1997: *Seasonal Variability of Mixed Layer Depth for the World Ocean.* NOAA Atlas NESDIS 14, 96 pp.

Moorthi, S., H.-L. Pan, and P. Caplan, 2001: Changes to the 2001 NCEP operational MRF/AVN global analysis/forecast system. NWS Tech. Procedures Bull. 484, 14 pp. [Available online at http://www.nws.noaa.gov/om/tpb/484.htm.]

Murtugudde, R., and A. J. Busalacchi, 1999: Interannual variability of the dynamics and thermodynamics of the tropical Indian Ocean. *J. Climate,* **12,** 2300–2326.

Pacanowski, R. C., and S. M. Griffies, 1998: *MOM 3.0 Manual.* NOAA/Geophysical Fluid Dynamics Laboratory, 668 pp.

Pan, H.-L., and L. Mahrt, 1987: Interaction between soil hydrology and boundary layer developments. *Bound.-Layer Meteor.,* **38,** 185–202.

Reynolds, R. W., N. A. Rayner, T. M. Smith, D. C. Stokes, and W. Wang, 2002: An improved in situ and satellite SST analysis for climate. *J. Climate,* **15,** 1609–1625.

Saha, S., and Coauthors, 2006: The NCEP Climate Forecast System. *J. Climate,* **19,** 3483–3517.

——, and Coauthors, 2013: The NCEP Climate Forecast System version 2. *J. Climate,* in press.

Saji, N. H., B. N. Goswami, P. N. Vinayachandran, and T. Yamagata, 1999: A dipole mode in the tropical Indian Ocean. *Nature,* **401,** 360–363.

Schott, F. A., S.-P. Xie, and J. P. McCreary Jr., 2009: Indian Ocean circulation and climate variability. *Rev. Geophys.,* **47,** RG1002, doi:10.1029/2007RG000245.

Trenberth, K. E., G. W. Branstator, D. J. Karoly, A. Kumar, N. C. Lau, and C. Ropelewski, 1998: Progress during TOGA in understanding and modeling global teleconnections associated with tropical sea surface temperatures. *J. Geophys. Res.,* **103** (C7), 14 291–14 324.

Wang, H., and R. Fu, 2000: Winter monthly mean atmospheric anomalies over the North Pacific and North America associated with El Niño SSTs. *J. Climate,* **13,** 3435–3447.

——, A. Kumar, W. Wang, and Y. Xue, 2012a: Seasonality of the Pacific decadal oscillation. *J. Climate,* **25,** 25–38.

——, ——, ——, and ——, 2012b: Influence of ENSO on Pacific decadal variability: An analysis based on the NCEP Climate Forecast System. *J. Climate,* **25,** 6136–6151.

Wang, W., M. Chen, and A. Kumar, 2010: An assessment of the CFS real-time seasonal forecasts. *Wea. Forecasting,* **25,** 950–969.

Wyrtki, K., 1973: An equatorial jet in the Indian Ocean. *Science,* **181,** 262–264.

Xie, S.-P., H. Annamalai, F. A. Schott, and J. P. McCreary Jr., 2002: Structure and mechanisms of South Indian Ocean climate variability. *J. Climate,* **15,** 864–878.

——, K. Hu, J. Hafner, H. Tokinaga, Y. Du, G. Huang, and T. Sampe, 2009: Indian Ocean capacitor effect on Indo–western Pacific climate during the summer following El Niño. *J. Climate,* **22,** 730–747.

Xue, Y., and Coauthors, 2012: A comparative analysis of upper-ocean heat content variability from an ensemble of operational ocean reanalyses. *J. Climate,* **25,** 6905–6929.

Zebiak, S. E., and M. A. Cane, 1987: A model El Niño–Southern Oscillation. *Mon. Wea. Rev.,* **115,** 2262–2278.

Zhang, M. H., R. D. Cess, and S. C. Xie, 1996: Relationship between cloud radiative forcing and sea surface temperatures over the entire tropical oceans. *J. Climate,* **9,** 1374–1384.